Plasma Sources
Science and
Technology

PURPOSE-LED
PUBLISHING™

ACCEPTED MANUSCRIPT

Temporal evolution and breakdown mechanisms of synthetic air gap under lightning impulse

To cite this article before publication: Shenli Jia *et al* 2025 *Plasma Sources Sci. Technol.* in press https://doi.org/10.1088/1361-6595/ae2efe

Manuscript version: Accepted Manuscript

Accepted Manuscript is “the version of the article accepted for publication including all changes made as a result of the peer review process, and which may also include the addition to the article by IOP Publishing of a header, an article ID, a cover sheet and/or an ‘Accepted Manuscript’ watermark, but excluding any other editing, typesetting or other changes made by IOP Publishing and/or its licensors”

This Accepted Manuscript is **© 2025 IOP Publishing Ltd. All rights, including for text and data mining, AI training, and similar technologies, are reserved.**.

During the embargo period (the 12 month period from the publication of the Version of Record of this article), the Accepted Manuscript is fully protected by copyright and cannot be reused or reposted elsewhere.

As the Version of Record of this article is going to be / has been published on a subscription basis, this Accepted Manuscript will be available for reuse under a CC BY-NC-ND 4.0 licence after the 12 month embargo period.

After the embargo period, everyone is permitted to use copy and redistribute this article for non-commercial purposes only, provided that they adhere to all the terms of the licence https://creativecommons.org/licences/by-nc-nd/4.0

Although reasonable endeavours have been taken to obtain all necessary permissions from third parties to include their copyrighted content within this article, their full citation and copyright line may not be present in this Accepted Manuscript version. Before using any content from this article, please refer to the Version of Record on IOPscience once published for full citation and copyright details, as permissions may be required. All third party content is fully copyright protected, unless specifically stated otherwise in the figure caption in the Version of Record.

View the article online for updates and enhancements.

This content was downloaded from IP address 202.200.236.180 on 26/12/2025 at 03:49

Temporal evolution and breakdown mechanisms of synthetic air gap under lightning impulse

Shenli Jia[1], Weihao Liu[1], Jinsong Wu[1], Junyu Lu[1], Xiaolong Huang[1], Wenjun Ning[1], Saikang Shen[1]*

(1. College of Electrical Engineering, Sichuan University, Chengdu 610065, China)

*Saikang Shen is the corresponding author.

Email: saikangshen@scu.edu.cn

Abstract: Synthetic air, owing to its environmental advantages, exhibits broad application prospects in high-voltage equipment. Although its breakdown characteristics under lightning impulses have been extensively investigated, systematic studies on the insulation performance and discharge processes of typical electrode configurations in GIS remain insufficient, and the temporal evolution and underlying mechanisms of the discharge process have yet to be elucidated. In this study, a combination of high-speed photography, intensified charge-coupled device (ICCD) imaging, voltage–current waveforms, and optical emission spectroscopy (OES) is employed to investigate the discharge characteristics in a rod-to-plane gap under lightning impulses at atmospheric pressure. Furthermore, a coupled 2D-0D simulation model is developed to elucidate the mechanism of lightning impulse breakdown process. Experimental results indicate that the discharge undergoes streamer followed by spark under lightning impulse. During the streamer phase, the emission spectrum is dominated by N_2(C-B) bands, with rotational temperatures ranging from 302.84 to 342.76 K. The spark phase exhibits prominent N^+ and O^+ lines, indicating extensive dissociation of gas molecules into atomic species, with gas temperatures rising to 38 875-39 118K and electron densities reaching 9.51×10^{23}-9.53×10^{23} m^{-3}. Simulation results further reveal that at a lower voltage (58 kV, 90 % $U_{50\%}$), electron generation is primarily driven by oxygen detachment from negative ions (O_3^-, O_2^-), while electron loss is dominated by attachment reactions. As the applied voltage increases to 97 kV

(150 % U_{50}%) and 129 kV (200 % $U_{50\%}$), the role of excited-state molecules and atoms in the ionization process is markedly enhanced, leading to a two-orders-of-magnitude rise in electron density and gas temperatures reaching tens of thousands of kelvins within 1 ns, ultimately resulting in spark formation. This work provides a detailed temporal evolution and mechanistic analysis of lightning impulse breakdown in synthetic air, offering valuable insights to guide the insulation design of environmentally friendly high-voltage equipment.

Keywords: Synthetic air, lightning impulse breakdown, Rod-plane discharge, Streamer, Spark, coupled 2D-0D coupled simulation

1 Introduction

SF_6 has excellent insulating and arc-quenching properties. It is widely used in gas insulated switchgear (GIS) and gas insulated transmission line (GIL). However, SF_6 exhibits an extremely high greenhouse effect, with a global warming potential (GWP) 25200 times that of CO_2 [1-5]. In California, the CARB regulation phases out the acquisition of new SF_6 gas-insulated equipment in stages, with the last category (≥245 kV) phased out by 2033. Existing equipment can remain in service, and exemptions apply [6]. The EU F-gas Regulation (EU 2024/573) phases out fluorinated gases according to voltage class. Equipment rated ≤24 kV and 24-52 kV must cease using fluorinated gases by 2026 and 2030, respectively. Higher-voltage equipment (52 – 145 kV and >145 kV) may use gases with a global warming potential (GWP) below 1 starting from 2028 and 2032, respectively. Derogations apply where no technically feasible solution is available or where lower life-cycle CO_2 equivalent emission solutions are available as per eco-design requirements [7]. Synthetic air, comprising N_2 and O_2 in a 4:1 ratio, has a GWP of zero and is environmentally benign. Although its dielectric strength is lower than that of SF_6, the required insulation levels can be achieved by increasing the internal gas pressure of the equipment [9-14]. At present, a 145 kV GIS using synthetic air insulation has been delivered in Finland. The world's first 252 kV synthetic air-insulated vacuum circuit breaker has also been successfully commissioned in Guangzhou, China, while an environmentally friendly GIS at the 550 kV level is still under development.

Gas breakdown induced by lightning impulse is one of the major threats to the reliable operation of high-voltage equipment. In 1937, Meek, Raether, and Loeb propose the streamer breakdown theory [15]. However, owing to its complexity, research into the breakdown mechanisms, streamers, and their development remains ongoing. A spatiotemporally resolved discharge observation system is developed at Chemnitz University of Technology [16] to investigate the breakdown mechanism of lightning impulse discharges across a 4 m gap. The study shows that the long-gap lightning impulse discharge is initiated by a primary streamer triggered by the rising applied voltage. During the propagation of this streamer, field weakening and the absence of ionization activity in the central region of the gap force the primary streamer to extinguish. As the applied voltage rises, the secondary streamer originates at the anode. When the ionization front reaches a position approximately 50 cm from the cathode, the accumulation of positive ions near the cathode establishes a strong local electric field, inducing electron emission from the cathode and generating a reverse-propagating wave. Owing to the higher current density, increased ionization rate, and elevated gas temperature, a leader channel then forms at the anode, ultimately culminating in breakdown . Chen She [17] employ a four-frame ICCD camera to capture the development of the positive streamer in a 57 cm rod-plane gap under lightning impulse. The streamer heads exhibit a fireworks-like, diffuse morphology, distinct from the dendritic patterns recorded by conventional cameras. Analysis of the observational data further reveals that higher voltage amplitudes and larger electrode dimensions lead to increased propagation velocities. In air-gap lightning impulse tests, Arik Subhana [18] speculates that the observed increase in breakdown voltage may be attributable to electronegative by-products such as O_3. These species are believed to influence the breakdown process by reducing the initial electron density. Currently, a substantial body of literature has provided in-depth statistical analyses and elucidated the development of long-gap lightning impulse discharges. However, the microscopic mechanisms of discharge initiation and mode transition under lightning impulses have not yet been clearly elucidated. Moreover, the extremely long rise time of the standard lightning impulse waveform (1.2 μs) markedly increases the stochasticity of the rod-plane discharge process. Under short-gap conditions, capturing these transient evolutions is particularly challenging. Consequently, existing research on short-gap lightning impulse discharges has largely been confined to statistical analyses of macroscopic parameters such as breakdown voltage, and systematic studies of the discharge dynamics and underlying microscopic evolution mechanisms are still required. With the increasing application of synthetic air in switching equipment, the investigation of breakdown characteristics and mechanisms in short gaps has become increasingly important. It should be noted that significant differences exist between the discharge mechanisms of long and short gaps. Long gaps typically undergo a multi-stage evolution from streamer to leader to spark, with longer time scales and segmented development. In short gaps, the streamer and spark channels form almost instantaneously, and the mode transition occurs extremely rapidly. Therefore, the conclusions drawn from long-gap studies cannot be directly extrapolated to short-gap scenarios, and systematic investigations of short-gap discharges under lightning impulse are still required to elucidate their breakdown characteristics and underlying microscopic mechanisms.

The transition from streamer to spark represents a critical stage in gas insulation failure. Although the streamer does not lead to immediate breakdown, its evolution governs the distribution of space charge and the formation of conductive channels, thereby establishing the conditions for subsequent spark. Once the streamer develops into a spark, the insulation is completely lost. Research on streamers and their developmental characteristics under nanosecond-pulse and direct-current (DC) has been continuously and intensively advanced through extensive numerical simulation studies. However, owing to the prolonged transition time from the streamer to the spark and the highly complex reaction processes involved under lightning impulse, related studies remain very limited. The mechanisms currently considered to trigger the streamer-to-spark transition include the electron-attachment-controlled mechanism, the chemical and stepwise ionization mechanism, and the gas-density-reduction mechanism. These mechanisms act by balancing electron-loss processes and ultimately accelerating ionization reactions, thereby inducing the streamer-to-spark transition [19].

Zhang Bin et al. employ a 2D model to simulate the streamer -to-filament transition in nanosecond-pulse discharges at atmospheric pressure. Once a conductive channel forms within the discharge gap, both streamer and filament phases appear within a few nanoseconds, with two filaments originating from the anode and cathode, respectively. Concurrently, the gas temperature rose abruptly from 350 K to 2800 K. During this transition, the dissociation and ionization of molecular nitrogen excited states ($A^3\Sigma_u^+$, $B^3\Pi g$, $a'^1\Sigma_u^-$ and $C^3\Pi_u$), as well as the ionization of O and N in both ground and excited states, are found to play critical roles [20]. N. Minesi employs numerical simulations to investigate the air ionization mechanisms of nanosecond-pulse discharges under atmospheric. The discharge is found to undergo complete ionization and thermalization within less than 1 ns; the rapid ionization process is attributed to electron-impact collisions with excited states of O and N, while the swift thermalization results from elastic electron-ion collisions [21]. To date, the vast majority of numerical simulations of discharges have focused on nanosecond-pulse or DC. The few investigations of physical models for lightning impulse discharges have treated them as DC discharges or proportionally compressed them into the nanosecond-pulse timescale [22]. Such simplifications evidently overlook multiple processes and hinder the accurate reproduction of actual discharge characteristics.

This study systematically characterizes the morphological evolution, electrical characteristics, particle distribution, and temperature distribution of a 40 mm gap discharge under lightning impulse, employing high-speed photography, ICCD imaging, voltage and current waveform recording, and optical emission spectroscopy (OES). Thereafter, the transition from lightning impulse streamer to spark in synthetic air is simulated and analyzed based on a 2D streamer model and a 0D homogeneous plasma model. Finally, by integrating experimental observations and simulation results, the microscopic mechanisms underlying the streamer-to-spark transition at various voltage amplitudes are elucidated.

2 Experimental and simulation methods

2.1 Electro-optical combined diagnostic platform for discharge experiments

To investigate the development of discharges in a synthetic-air gap under lightning impulse, an electro-optical combined diagnostic platform is established (Fig. 1). The platform comprises four main components: the lightning impulse power supply, the gas-insulated experimental chamber, the electrical measurement system, and the optical diagnostic system.

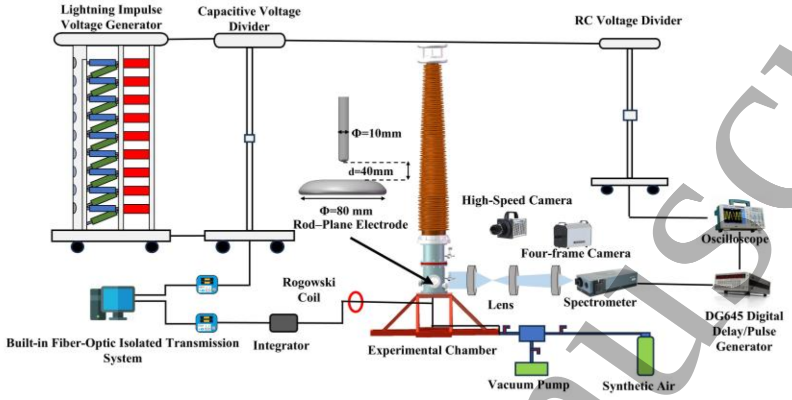

Fig. 1. Electro-optical combined diagnostic platform for lightning-impulse discharge experiments.

The experimental platform uses a 900 kV/72 kJ lightning impulse generator, which produces the standard positive lightning impulse waveform of 1.2/50 μs (Fig. 2). The synthetic air experimental chamber (equipped with rod-plane electrodes) is made of aluminum alloy. It includes three quartz glass optical windows, which have a transmittance of over 90% in the wavelength range of 170 nm to 2200 nm, meeting the requirements for optical measurements. This study uses synthetic air (N_2:O_2 = 4:1, purity 99.99 %) at 0.1 MPa.

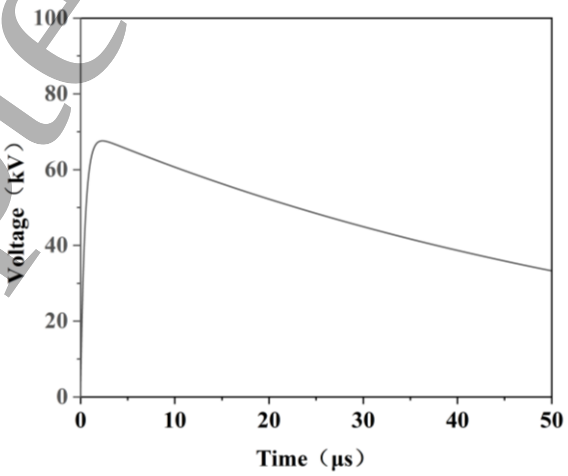

Fig 2. Standard lightning impulse voltage waveform (1.2/50 μs), with a front time of 1.2 μs and a time to half-value of 50 μs.

In the experiments, a 10 mm-diameter rod electrode and an 80 mm-diameter plane electrode are used, with a gap of 40 mm. The rod electrode terminates in a hemispherical tip whose radius equals the electrode diameter. Both electrodes are fabricated from aluminum alloy and are smooth finish and polished. f is employed to quantify the spatial non-uniformity of the electric field distribution and is defined as the ratio of the maximum field strength to the mean field strength, calculated as:

$$f = \frac{\boldsymbol{E}_{max}}{\boldsymbol{E}_{av}} \tag{1}$$

$$\boldsymbol{E}_{av} = \frac{U}{d} \tag{2}$$

In the equation, $\boldsymbol{E}_{max}$ is the maximum electric field strength in the rod-plane gap, $\boldsymbol{E}_{av}$ is the average field strength, and d denotes the electrode separation. The calculated f under the present experimental conditions is 6.08, indicating an extremely non-uniform field.

The optical diagnostic system comprises a four-frame camera (XIOPM-FC-AW-4, minimum exposure time 3 ns), a grating spectrograph with ICCD (Andor SR750-D1, minimum exposure time 2 ns), a high-speed camera (ACS-3 M16), a digital oscilloscope (Tektronix MDO310), and a DG645 delay generator (Stanford Research Systems). When the lightning impulse source applies voltage, the divider's rising-edge signal is sent to the oscilloscope, which samples and trigger the DG645. The DG645 then sends a trigger signal to initiate image acquisition. Because streamer emission is extremely weak, an optical collection system of three biconvex lenses (diameter 50.8 mm; focal lengths f = 100 mm, 200 mm, and 300 mm) is employed. This lens assembly collects the streamer light and focuses it onto the spectrograph slit for spectral acquisition.

Voltage and current are measured using a divider (2000 : 1) and a Rogowski coil (CPHX 9300A, 100MHz, measuring limit is 3000 A). The discharge circuit and the measurement circuit are isolated by an HBM ISOBE5600t fiber-optic transmission system to minimize signal interference. The 50% breakdown voltage ($U_{50\%}$) is determined in accordance with IEC 60060-1. During the step-up/step-down test, 20 breakdown events are recorded to establish $U_{50\%}$ under lightning-impulse (voltage increment of 1 kV, interval of 5 min), and $U_{50\%}$ is then obtained by fitting the breakdown statistics to a Weibull distribution. $U_{50\%}$ as a key benchmark for evaluating the streamer-to-spark transition under lightning impulses. Under the experimental conditions of this study, the 100% $U_{50\%}$ corresponds to 64.5 kV.

2.2 Model Description

2.2.1 Streamer Discharge Model

As shown in Fig. 3, a 2D axisymmetric streamer model in a rod-plane gap is established, comprising the high-voltage electrode (rod), the grounded electrode (plane), and the plasma region. The rod electrode has a diameter of 10 mm and a tip curvature radius of 5 mm. The rod-plane gap is filled with synthetic air (N_2:O_2 = 4 : 1) at atmosphere and 300 K. The model boundary conditions are identical to those in [23]. The model employs adaptive mesh refinement in a 2D axisymmetric coordinate system. The refinement criteria are based on electron density, and the detailed mesh-optimization strategy is described in [23]. The external circuit parameters in the simulation follow the actual experimental design to generate a lightning impulse waveform that conforms to IEC 60060-1 and couple it with the plasma. The external-circuit module solves the ordinary differential equations (ODEs) in the time domain to obtain the circuit voltage and current in real time and supplies these data as boundary conditions for the Poisson equation in the plasma module.

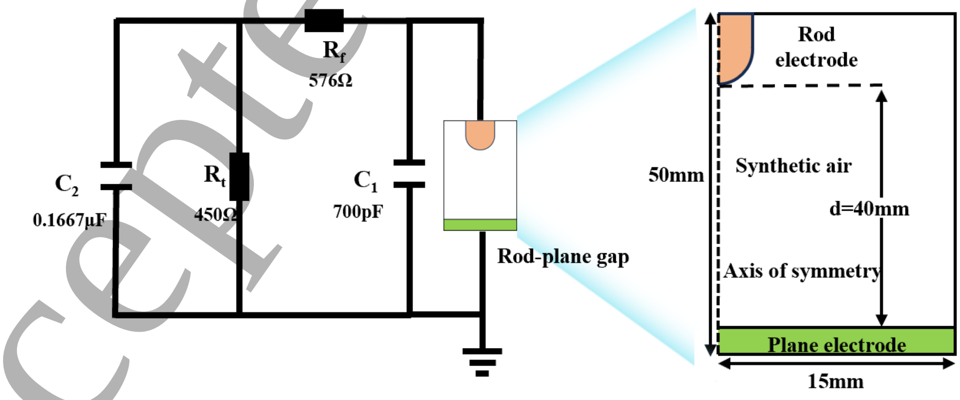

Fig 3. 2D axisymmetric simulation model coupled with the external circuit.

The 2D plasma fluid code PASSKEy2 is used in this study to simulate streamer under lightning impulse [24, 25]. This code has been validated against experimental measurements of discharge morphology, propagation velocity, and voltage-current waveforms [26,27]. The drift-diffusion equation for species in the fluid model is:

$$\frac{\partial n_i}{\partial t} + \nabla \cdot \mathbf{\Gamma}_i = S_i + S_{\mathrm{ph}}, i = 1, 2, \ldots, N_{\mathrm{total}} \tag{3}$$

where n_{i} is the number density of species i, t is time, S_i is the reaction source term for species i, and S_{ph} is the photoionization source term. Γ_i is the plasma flux of species i due to drift and diffusion, which is expressed as:

$$\mathbf{\Gamma}_i = \left(q_i / \left|q_i\right|\right) \mu_i n_i \mathbf{E} - D_i \nabla n_i, i = 1, 2, \ldots, N_{\mathrm{charge}} \tag{4}$$

where q_i is the charge number of species i, D_i is its diffusion coefficient, μ_i is the mobility of species i, and E denotes the electric field. The electron diffusion coefficient and mobility are calculated using BOLSIG+[28]. Electron swarm parameters and the rate coefficients of electron-collision reactions are expressed as explicit functions of the reduced electric field (E/N). The kinetic mechanism of synthetic air in the 2D model is established based on References [26] and [29], comprising 16 species and 38 reactions. The accuracy of this mechanism has been validated in the relevant literature [26, 27]. Gas density and temperature variations are calculated and updated by solving the Euler equations. The coupling strategy between the plasma equations and the Euler equations is described in detail in Reference [30]. To initiate the streamer discharge, a uniform electron and ion number density of 10^{10} m^{-3} is imposed in the model [31-35].

2.2.2 Streamer-to-spark transition model

The transition time from streamer to spark in the lightning impulse may require several microseconds, making 2D simulations impractical for such long durations. Moreover, the transition involves numerous reactions, and employing simplified kinetic schemes omits important information. Therefore, a 0D global model is employed, assuming that once the streamer forms an ionization channel, the cross-sectional average values of all species within the quasi-neutral region can be described by the 0D model [29]. Compared with previous studies, the present model features several important improvements. It incorporates a more comprehensive set of reaction kinetics, thereby avoiding the loss of critical information associated with simplified models. It also implements real-time updates of the system temperature during simulations, which more accurately capture the effects of energy deposition and gas heating on discharge evolution. In addition, by employing a 0D framework, it enables microsecond-scale simulations, thus overcoming the limitations of 2D models in long-time calculations.

This study uses CPCC, a homogeneous plasma reaction kinetics calculation tool built upon the ZDPlaskin code and a sensitivity analysis module, to perform 0D calculations [36, 37, 38]. It dynamically solves the electron energy distribution function (EEDF) and the temporal evolution of the densities of electrons, excited species, and ions in the plasma discharge system, and calculates the gas temperature based on reaction enthalpies. The kinetic scheme in this study incorporates 58 species and 877 reactions in synthetic air. The EEDF calculation takes into account processes such as dissociation, ionization, and superelastic collisions. When the degree of ionization exceeds 10^{-5}, electron–electron collisions are included. All other BOLSIG+ parameters remain at their default values [28]. The 0D model also specifically includes electron-impact ionization and excitation reactions of molecular excited states ($N_2(A^3\Sigma_u^+)$, $N_2(B^3\Pi g)$, $N_2(C^3\Pi_u)$, $N_2(a'^1\Sigma_u^-)$ and $O_2(a^1\Delta g)$) and atomic excited states ($N(^4D^0, 3p)$, $N(^2S^0, 3p)$, $N(^4P, 2s^22p^4)$, $N(^2P, 3s)$, $N(^4P,3s)$, $N(^2D)$, $N(^2P)$, $O(^1D)$ and $O(^1S)$)[21, 39, 40]. In the model, only the ionization rates of the ground-state ions N^+ (^3P) and O^+ (^4S) are calculated, since ionization into other excited states is negligible [39, 40].

Table 1. Particle species considered in the 0 D model.

Particle category	Particle
Monatomic particles.	N, $N(^4D^0, 3p)$, $N(^2S^0, 3p)$, $N(^4P, 2s^22p^4)$, $N(^2P, 3s)$, $N(^4P,3s)$, $N(^2D)$, $N(^2P)$, O, $O(^1D)$, $O(^1S)$
Ground and excited states of N_2 and O_2	N_2, $N_2(A^3\Sigma_u^+)$, $N_2(B^3\Pi g)$, $N_2(a'^1\Sigma_u^-)$, $N_2(C^3\Pi_u)$ $N_2(v1)$, $N_2(v2)$, $N_2(v3)$, $N_2(v4)$, $N_2(v5)$ $N_2(v6)$, $N_2(v7)$, $N_2(v8)$, O_2, $O_2(a^1\Delta g)$, $O_2(B^1\Sigma g^+)$ $O_2(4.5eV)$ $O_2(v1)$, $O_2(v2)$, $O_2(v3)$, $O_2(v4)$
Ground-state neutral particles	O_3, NO, N_2O, NO_2, NO_3, N_2O_5
Ions	N^+, N_2^+, N_3^+, N_4^+, O^+, O_2^+, O_4^+, O^-, O_2^-, O_3^-,

	O_4^-, NO^+, N_2O^+, NO_2^+, NO^-, N_2O^-, NO_2^-, NO_3^-
Cluster and Electron	$O_2^+ \cdot N_2$, E

The 0D model is used to study the evolution of species at the center point (r = 0, z = 20 mm) of the rod-plane electrode gap following the streamer. To satisfy the spatial uniformity assumption of the 0D model, the initial time is defined as the moment when the ionization front first passes this fixed point, thereby avoiding disruption of the model by strong convective effects. The Laplace field derived from the experimental waveform serves as the electric field input. Initial electron density and gas temperature are extracted directly from the 2D simulations.

3 Results and discussion

3.1 Experimental results

3.1.1 Morphological study of rod-plane discharge under lightning impulse

Fig 4 shows high-speed camera images of streamer morphology under positive lightning impulse of different amplitudes (frame exposure time: 33 μs, sufficient to capture the entire streamer process). The streamers in the images originate not only from the tip of the rod electrode but also emerge around its periphery due to field enhancement at the electrode's sharp edges. The brighter channels observed near the rod electrode are consistent with the findings in [41], which attribute such features to secondary streamers developing after the primary streamer has traversed the gap. As the voltage increases from 52 kV to 62 kV, the number of streamer branches increases, and both the emission intensity and the length of the secondary streamers are significantly enhanced. In addition to branching at the tip of the rod electrode, streamer branching also occurs at the streamer head during propagation (as indicated by the red circle in Fig 4b). Nijdam et al. attribute branching during streamer propagation primarily to random fluctuations of the streamer head. Increasing the photoionization rate reduces these random fluctuations, thus yielding a streamer morphology with fewer branches [42]. Fig. 4 also shows that some branched channels are relatively thin and stop developing before reaching the cathode plane. These channels are referred to as arrested streamers [43]. This phenomenon indicates that the electric-field enhancement at the heads of some streamers is insufficient to sustain their further propagation [44].

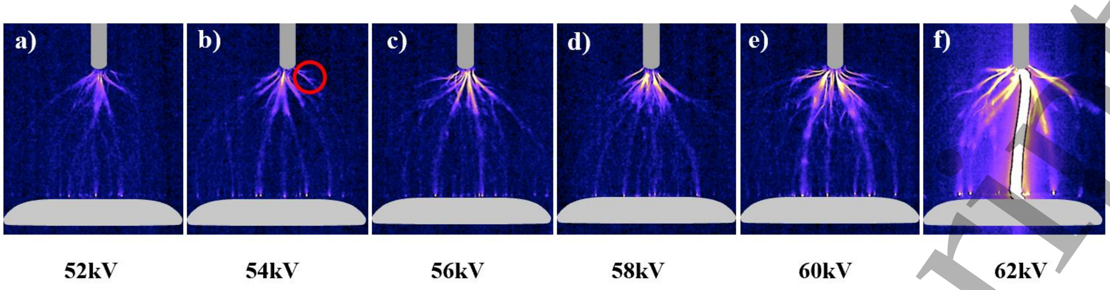

Fig 4. Images of streamer under lightning impulse of varying amplitudes until spark breakdown (synthetic air pressure: 0.1 MPa; rod-plane gap: 40 mm; exposure time: 0.6-33.6 μs after the application of the lightning impulse (time 0 corresponds to the voltage rise onset)). The red circle in panel (b) indicates the occurrence of streamer branching at the streamer head.

Due to the limited temporal resolution of the high-speed camera, capturing the evolution of a streamer within a single discharge is difficult. Therefore, this study employs a four-frame camera to record the development of an individual streamer (exposure time per frame: 30 ns). The luminous trajectory captured by the four-frame camera corresponds to the propagation path of the streamer head. As shown in Fig. 5 (a), under short-exposure conditions the streamer head exhibits a firework-like morphology, in contrast to the dendritic form captured by the high-speed camera. Under the 97 kV (150% $U_{50\%}$) lightning impulse, the strong electric field at the rod electrode triggers electron avalanches. As these electrons then drift towards the rod electrode, they continuously induce collisional ionization, thereby extending the plasma region and forming multiple bright streamer channels. In the first frame (Fig. 5 (b1)), the streamer has traversed the gap and the channel brightness diminishes. In the second frame (Fig. 5(b2)), the original streamer disappears and a new one forms at the rod electrode. As the voltage increases further, the new streamer develops almost along the initial streamer path, with its brightness slightly exceeding that of the initial streamer (Fig. 5 (b3) and (b4)). As shown in Fig. 6 (a), when the voltage increases to 129 kV (200% $U_{50\%}$), the streamer appears earlier. In the first frame (Fig. 6 (b1)), when the new streamer just emerges, the residual image of the previous streamer is still visible. In the second frame (Fig. 6 (b2)), the streamer has already bridged the gap. In the third and fourth frames (Fig. 6 (b3) and (b4)), a new streamer with stronger light intensity appears again, exhibiting behavior similar to that observed under the 97 kV. Since the camera can only record 2D images, some streamers may develop in front of or behind the primary channel. The superposition of their emission intensities in the image may also lead to the observed brightness enhancement. The long-exposure image (Fig. 4 and Fig. 7), which shows numerous streamer channels in each frame, differs significantly from the short-exposure image (Fig. 5 and Fig. 6), where only a few streamers appear in each frame. This observation indicates that, under the lightning impulse, the streamer channels may not all appear at the same moment due to the stochastic nature of the discharge.

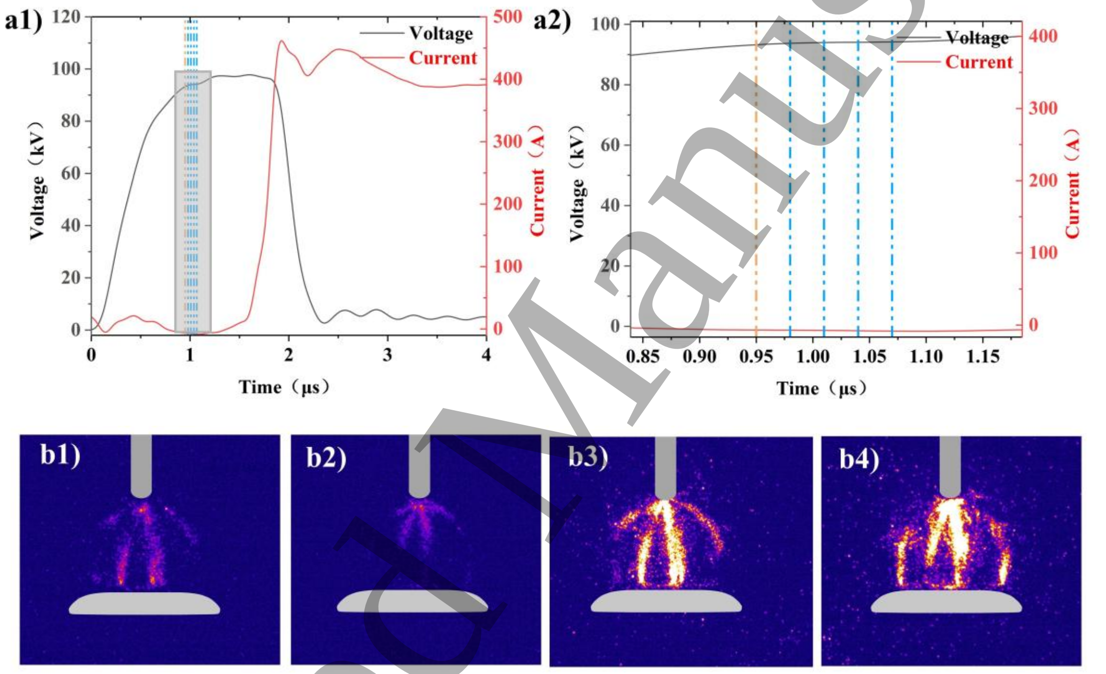

Fig 5. Optical evolution and electrical characteristics of streamer in a rod-plane gap at 97 kV. (a) Voltage and current waveforms synchronously recorded during four-frame camera imaging. The orange vertical line indicates the trigger time of the first frame, and the blue vertical lines indicate the trigger times of the remaining three frames. Figure (a2) is an enlarged view of the region marked by the gray box in Figure (a1). (b) Sequential images of streamers between the rod electrode (anode) and the plane electrode (cathode) captured by the four-frame camera, with an exposure time of 30 ns for each frame. The intensifier voltage of the camera is set to 764 V, and the gain value is 8000.

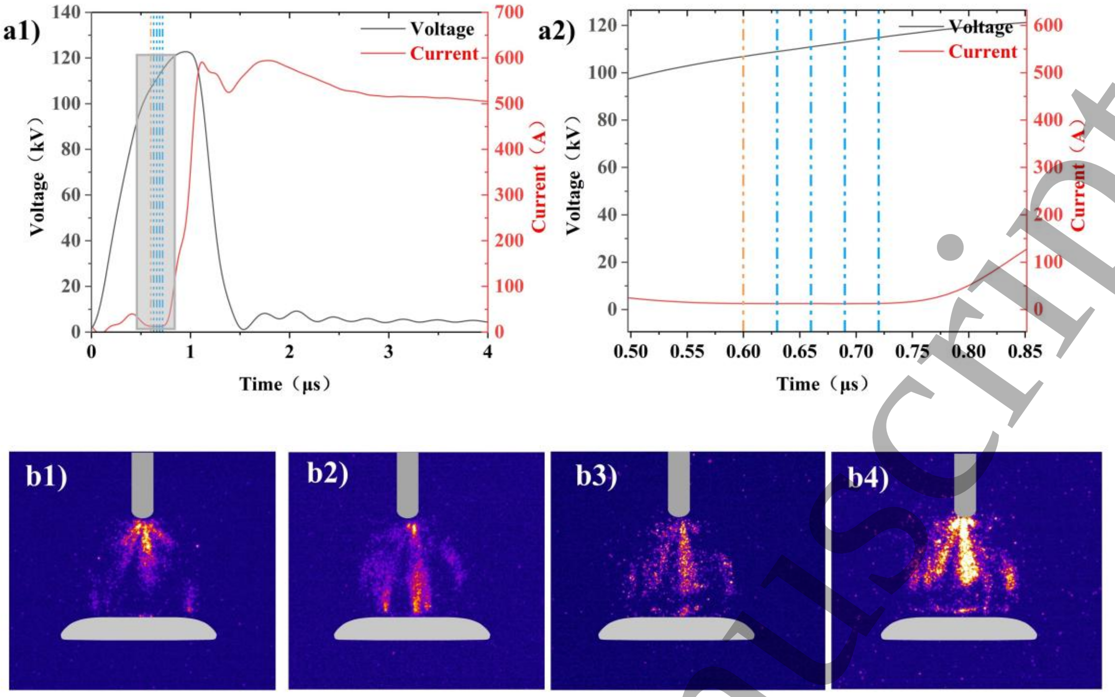

Fig 6. Optical evolution and electrical characteristics of streamer in a rod-plane gap at 129 kV. (a) Voltage and current waveforms synchronously recorded during four-frame camera imaging. The orange vertical line indicates the trigger time of the first frame, and the blue vertical lines indicate the trigger times of the remaining three frames. Figure (a2) is an enlarged view of the region marked by the gray box in Figure (a1). (b) Sequential images of streamers between the rod electrode (anode) and the plane electrode (cathode) captured by the four-frame camera, with an exposure time of 30 ns for each frame. The intensifier voltage of the camera is set to 764 V, and the gain value is 8000.

At lightning impulse of 97 kV and 129kV, the transition from streamer to spark may last from several hundred nanoseconds to microseconds. Fig 7 (a) shows the streamer-to-spark transition continuously captured by the four-frame camera when the 97 kV lightning impulse is applied (exposure time per frame: 500 ns). In the first frame after camera triggering, numerous streamer channels appear. In the second frame, the streamer light intensity is markedly reduced, yet filamentary luminous channels remain visible. In the third and fourth frames, one of the filamentary luminous channels observed earlier eventually evolved into a spark. As shown in Fig. 7 (b), when the applied voltage is increased to 129 kV, the streamer-to-spark transition is significantly accelerated, and the streamer channels become thicker and brighter. Ultimately, one of the streamer channels evolves into a spark channel.

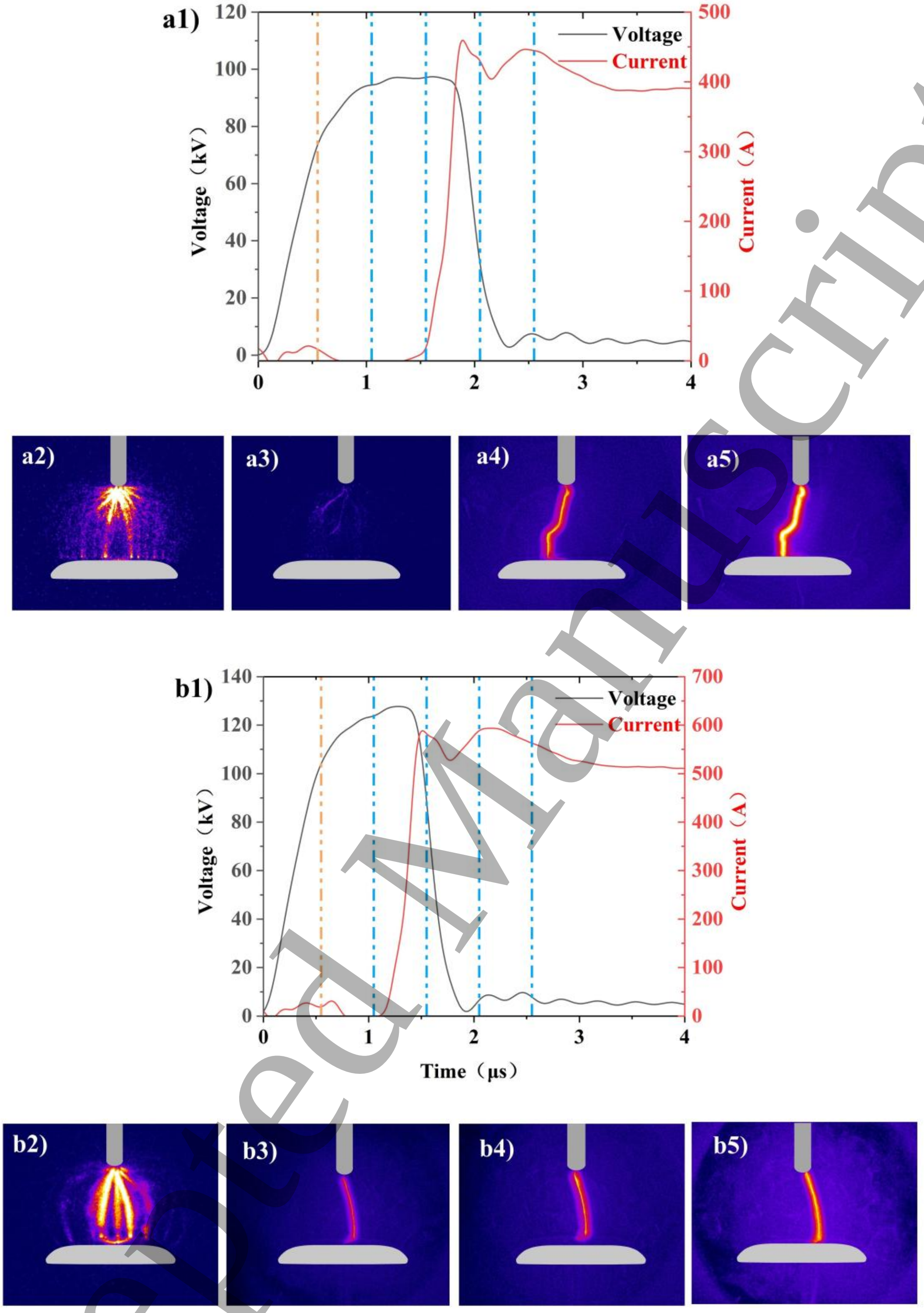

Fig 7. Sequential imaging of the streamer-to-spark transition between the rod (anode) and the plane (cathode) is performed with the four-frame camera, with each frame exposed for 500 ns. The intensifier voltage of the camera is set to 764 V, and the gain value is 8000. The orange vertical line indicates the trigger time of the first frame, and the blue vertical lines indicate the trigger times of the remaining three frames.
(a) Applied voltage: 97 kV. (b) Applied voltage: 129 kV.

It should be noted that, under nanosecond pulse, the dependence of gas breakdown time on applied voltage, gap distance, and gas type has been revealed in the study by Felsenthal and Proud [45]. In this section, nanosecond time-resolved optical observations under lightning impulse (microsecond pulse) captured the transition process from streamer to spark, thereby deepening the understanding of the temporal evolution characteristics of discharge under lightning impulse. Owing to the stochastic nature of the lightning-impulse discharge, streamer channels may not all appear at the same moment. Under the present experimental conditions (40 mm rod-to-plane gap, 0.1 MPa synthetic air, and standard lightning impulse peak voltages of 97 kV and 129 kV), the transition from streamer to spark occurred on a sub-microsecond to microsecond timescale and was significantly accelerated with increasing applied voltage. This behavior is consistent with the findings of Felsenthal et al. under nanosecond pulse.

3.1.2 OES of rod-plane discharge

Measuring the OES during the lightning impulse process with a spectrometer can further elucidate the discharge mechanisms. The recorded streamer discharge emission spectra span a wavelength range of 350–700 nm with a resolution of 0.09 nm. In this experimental setup, the best achievable temperature resolution is ±11 K, and the actual measurement uncertainty may exceed this value. As shown in Fig. 8, under the lightning impulse voltage of 58 kV (90% $U_{50\%}$), the most intense emission bands occur at 350–450 nm and are associated with the second positive system (SPS) of N_2:

$$e+N_2\left(X^1\Sigma_g^+\right)\rightarrow e+N_2\left(C^3\Pi_u\right)$$

$$N_2\left(C^3\Pi_u\right)\rightarrow N_2\left(B^3\Pi_g\right)+h\nu$$

The identified spectral lines reflect electronic transitions in N_2 molecules from s-type multiplet orbitals to p-type multiplet orbitals. The OES of N_2 dominates in the positive streamer.

During the streamer phase, the OES toolbox package developed by Julian Held is applied to determine the rotational and vibrational temperatures by comparing theoretical and experimental N_2(C-B) emission spectra [46]. The temperature values are obtained by fitting the optical emission spectra using the software; therefore, no error values are indicated. Fig 8 shows the fitting results between the theoretical and experimental spectra over the 364.4–450.52 nm range. The rotational temperature of $N_2(C^3\Pi_u)$ molecules is measured to be 302.84–342.76 K, while the vibrational temperature ranges from 2356.97 K to 2880.74 K. Since rotational energy transfer is rapid at atmospheric pressure, the measured rotational temperature of $N_2(C^3\Pi_u)$ molecules can be regarded as equal to the gas temperature.

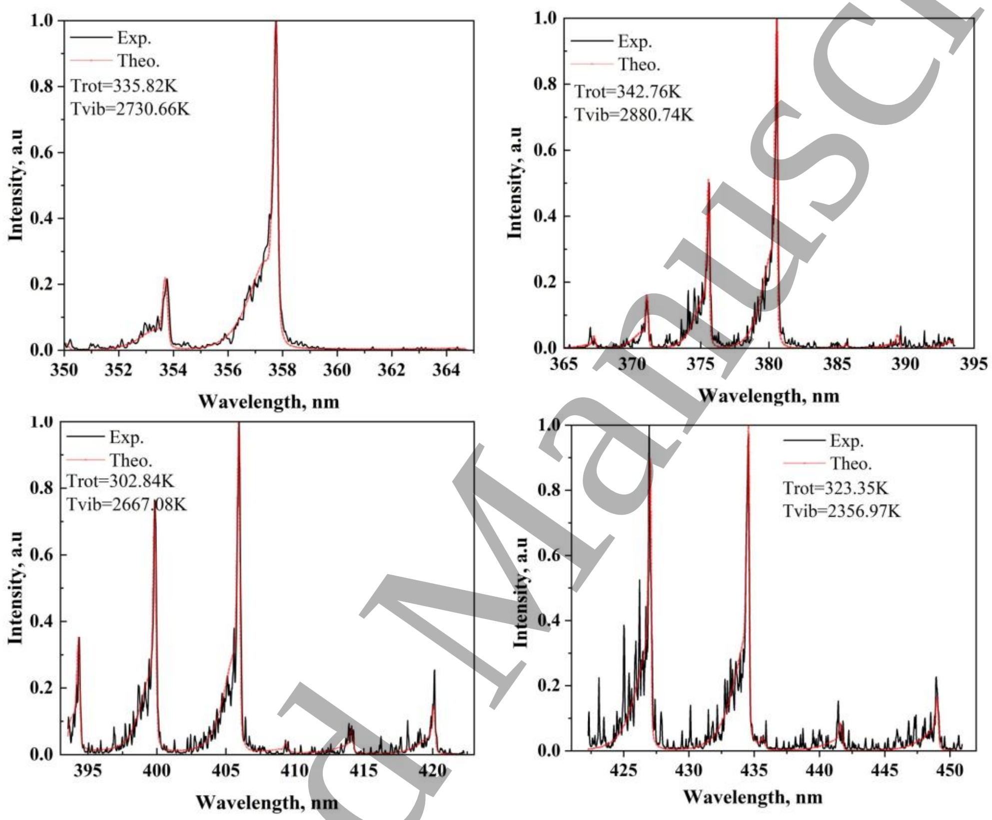

Fig 8. Experimental and theoretical emission spectra of the streamer under the 58 kV in the 350-450 nm range.

Fig 9 shows the OES in the 350–607 nm during the spark. Owing to the extremely high electron density, electron-impact excitation dominates, yielding pronounced Stark-broadened lines of N^+, O^+, N, and O. This indicates that molecules have been extensively dissociated into atoms, and the spectra are dominated by atomic emissions and continuum radiation.

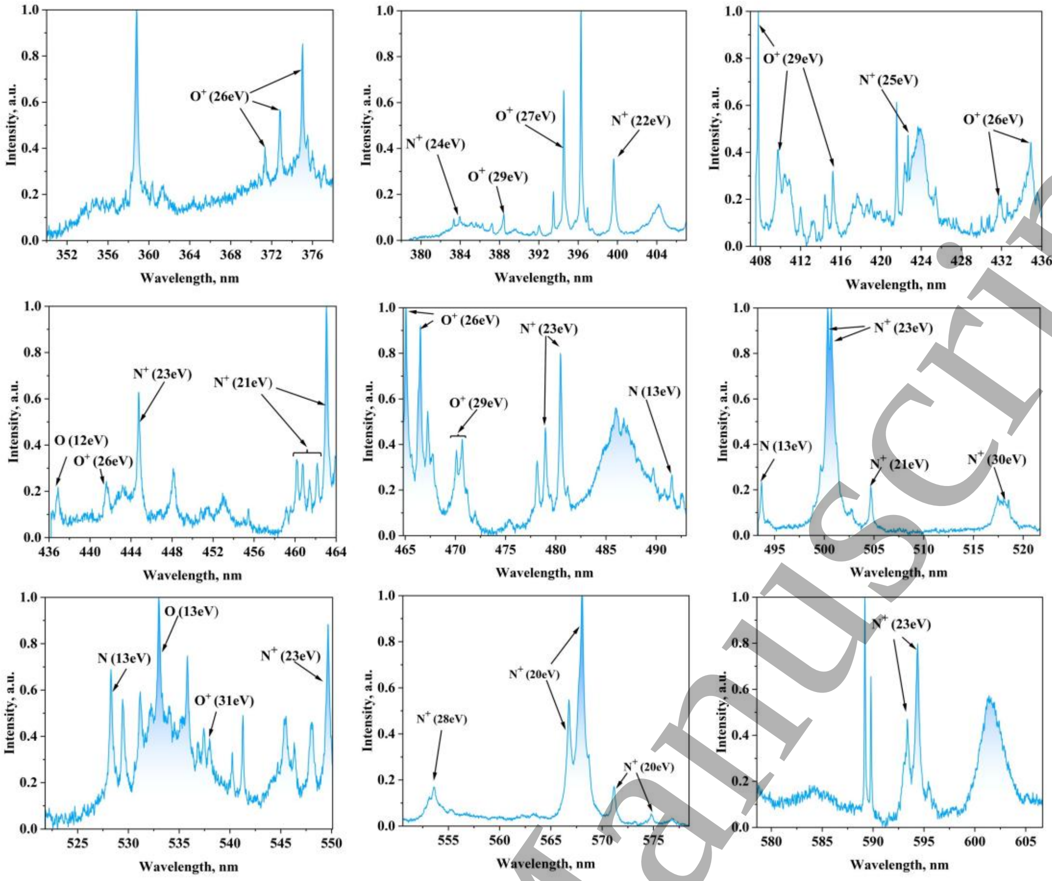

Fig 9. OES of the spark under a 97 kV.

During the spark phase, the plasma can be considered to be in local thermodynamic equilibrium (LTE). The temperatures of electron, ion, and gas are approximately equal, and thus the electron temperature is represented by the ion temperature. In Table 2, the intensities of three peaks in the N^+ emission spectrum are used to construct a Boltzmann plot of the upper energy levels, from which the excitation temperature of the nitrogen ions is derived. As shown in Fig. 10, the three peak data points are plotted on the Boltzmann diagram and the slope is calculated, yielding gas temperatures T of 38875K and 39118 K for 97 kV and 129 kV, respectively.

Table 2. Main singly ionized nitrogen lines used to analyze spark at 97 kV and 129 kV. Spectroscopic parameters are taken from the NIST database, where λ_k is the line center wavelength, A_k is the transition probability, g_k is the degeneracy of the upper level, and E_k and E_i are the energies of the upper and lower levels, respectively.

λ_k, nm	A_k, s^{-1}	E_i, eV	E_k, eV	g_k	$I_{U=150\%}$	$I_{U=200\%}$
500.515	1.14×10^8	20.666	23.142	9	21655	54682
504.51	3.37×10^7	18.483133	20.939965	3	4618	10636
517.952	1.07 × 108	27.746	30.139	11	3241	7793

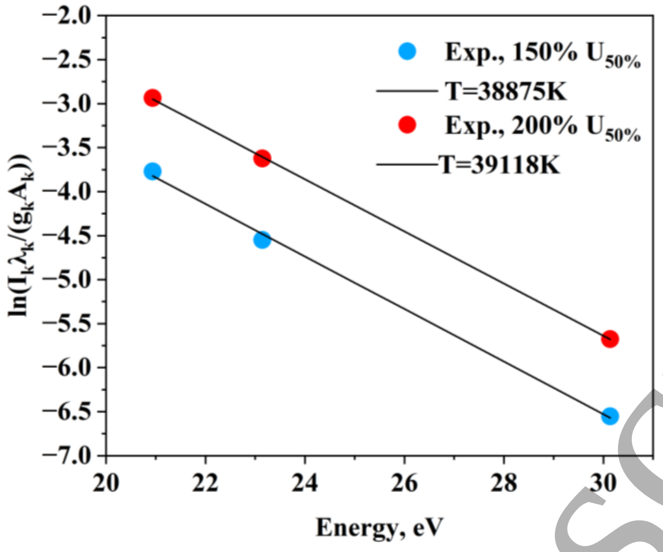

Fig 10. Boltzmann plots of N^+ spectral lines obtained at 97 kV and 129 kV, where I_k denotes the line intensity, λ_k the line center wavelength, A_k the transition probability, g_k the degeneracy of the upper level, and E_k the energy of the upper level. Each voltage condition corresponds to a single-shot optical emission spectrum measurement.

The observed atomic or ionic spectral line profiles arise primarily from the superposition of natural broadening, van der Waals broadening, Stark broadening, resonance broadening, instrumental broadening, and Doppler broadening. Under the present experimental conditions, Stark broadening induced by electron collisions predominates. Moreover, compared with the instrumental broadening of 0.0229 nm in this experiment, the effects of the other broadening mechanisms on the N^+ lines are negligible [47, 48]. At 504.51 nm, the half-width at half-maximum (HWHM) of the Stark broadening measured at 97 kV and 129 kV are 0.1343 nm and 0.1346 nm, respectively. Using the Stark parameters for N^+ lines listed by Konjević et al., the electron densities are calculated as 9.51×10^{23} m^{-3} and 9.53×10^{23} m^{-3}. The measurement uncertainty of the electron density arises primarily from the Stark parameters of the N^+ spectral lines provided in Reference [49], with an overall estimated uncertainty of less than 25% [47].

The OES results reveal the typical stage characteristics of synthetic-air short-gap discharges under lightning impulse. During the streamer, the emission spectra are dominated by the SPS of N_2, indicating that molecular excitations are the primary process. The measured rotational temperature is close to the room temperature, while the vibrational temperature rises significantly, suggesting that electron energy is mainly deposited in molecular excitation rather than bulk heating and that the plasma is in a non-equilibrium state. In the subsequent spark, the plasma exhibits features of near-local thermodynamic equilibrium, with both electron temperature and electron density reaching extremely high values. At this stage, the spectra are dominated by atomic and ionic lines of N, O, N^+, and O^+, reflecting extensive molecular dissociation. These findings highlight the coupled energy and particle dynamics during the streamer-to-spark transition under lightning impulse, providing experimental evidence for a deeper understanding of the discharge mechanisms and for guiding GIS insulation design.

3.2 Simulation Results

3.2.1 Evolution of streamer under lightning impulses of different amplitudes

Fig 11 shows the morphological characteristics of streamer at 58 kV, 97 kV, and 129 kV. The average propagation velocities of the streamers are 5.13×10^5 m/s, 5.88×10^5 m/s, and 6.67×10^5 m/s, respectively; the corresponding streamer diameters (full width at half maximum, FWHM) are 1756 μm, 2100 μm, and 2200 μm, respectively. Both the propagation velocity and diameter of the streamers increase with applied voltage.

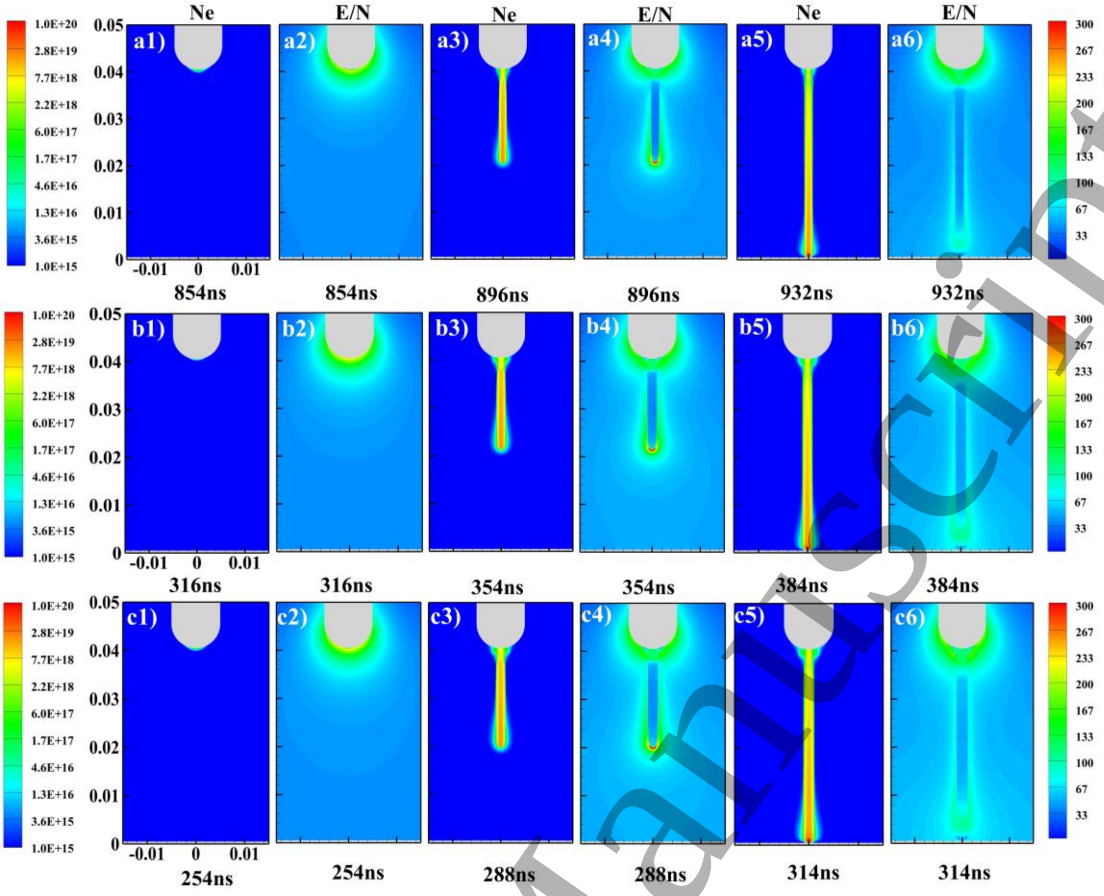

Fig 11. Electron density and electric field calculated at 58 kV (a1-a6), 97 kV (b1-b6), and 129 kV (c1-c6). The scales on both the x and y axes are in meters.

If the pulse rise time is extremely short and the amplitude exceeds the static breakdown voltage, the initial electron avalanche may occur immediately. However, the rise time of the lightning impulse is on the order of microseconds, resulting in a pronounced electron depletion process. Fig 12 shows the variation of electron density at different positions within the discharge gap under various voltages. After the external circuit applies the voltage, the preionization electrons in the gap undergo substantial drift and loss before effective collisional ionization occurs [50]. At voltages of 58 kV, 97 kV, and 129 kV, the electron depletion process near the anode persists for approximately 650 ns, 175 ns, and 125 ns, respectively. Concurrently, a transient electron-depleted region forms near the cathode, known as the electron clearing effect [51]. As the voltage continues to rise, the electric field strength near the rod electrode progressively increases, triggering electron avalanche reactions and causing a gradual rise in electron density. When the reduced electric field at the electrode tip further increases to approximately 200 Td (this field enhancement is also related to the increased ion number resulting from plasma reactions), a pronounced corona discharge occurs at the rod electrode tip, and the local electron density rapidly climbs to 1×10^{18} m^{-3}, marking the onset of the streamer. When the positive streamer reaches the cathode, a channel with an electric field strength of approximately 50 Td is established within the gap. It should be noted that the durations of these processes vary significantly with applied voltage. Compared to 58 kV, the electron depletion and avalanche processes at 97 kV and 129 kV proceed more rapidly and have shorter durations.

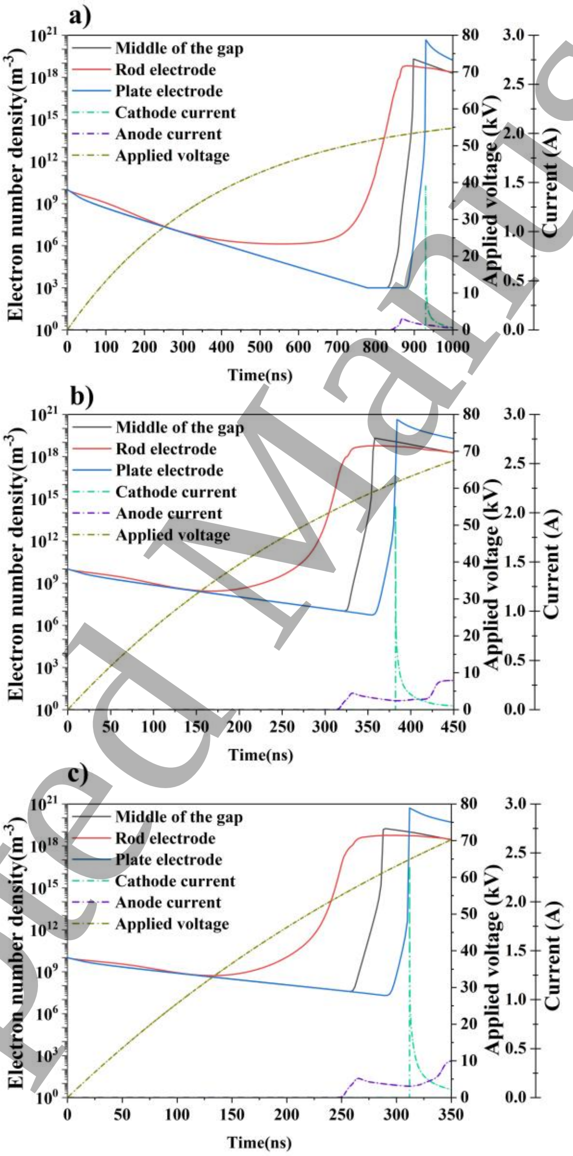

Fig 12. Temporal evolution of electron density at the gap center (r = 0, z = 20 mm), at the rod electrode, and at the plane electrode, along with the voltage and current, during the streamer process. (a) Applied voltage: 58 kV. (b) Applied voltage: 97 kV. (c) Applied voltage: 129 kV.

Fig 13 (a-b) shows the rate variations of the primary reactions along the electrode axis at 300 ns under voltages of 58 kV and 97 kV. At this time, no streamer has yet developed under either condition; this stage is dominated by the sequence of electron excitation, molecular energy transfer, and quenching. Electron collisions excite N_2 to the $N_2(B^3\Pi g)$ and $N_2(C^3\Pi_u)$ states, yielding excited-state molecules. These molecules then collide with neutral species, transferring energy into new excited states or directly inducing O_2 dissociation. The resulting O and $O(^1D)$ are quenched or proceed to subsequent reactions. At this stage, ionization reactions have not yet become dominant, and energy is concentrated in molecular excitation and nonradiative transfer. When the voltage is increased to 97 kV, at 300 ns the rates of all reactions increase markedly. Ground-state ionization of N_2 molecules also becomes one of the dominant reactions at this time. Fig 13 (c) shows the rate variations of the primary reactions along the electrode axis at 300 ns under the 129 kV. At this time, streamer has already commenced, and the ionization front rapidly generates large numbers of excited-state molecules and electrons, forming an channel and driving the swift propagation of the front. After the ionization front passes, the mean electron energy within the channel begins to decay and reaction rates decrease markedly. However, a high-rate region approximately 2.8 mm in length persists near the anode, with reaction rates approaching those at the ionization front. This high-rate region may be associated with the formation of the secondary streamer [52].

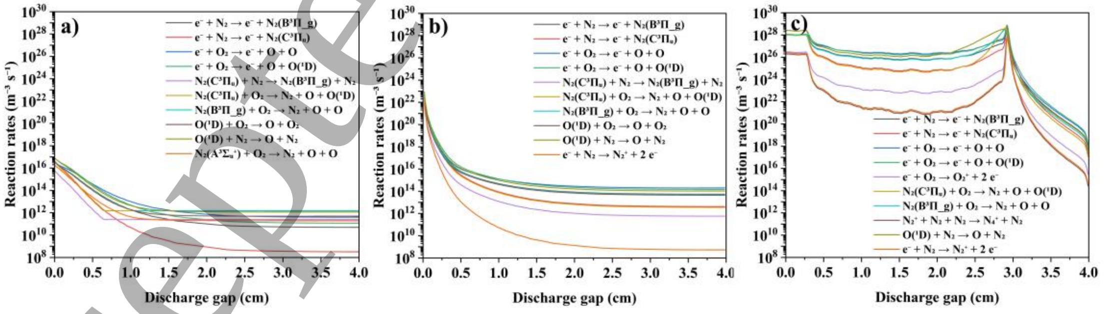

Fig 13. Variation of the main reaction rates along the electrode axis at 300 ns under different applied voltages. (a) Applied voltage: 58 kV. (b) Applied voltage: 97 kV. (c) Applied voltage: 129 kV.

Due to the relatively slow rise rate of the lightning impulse, the voltage after streamer channel formation remains close to the critical discharge voltage. The reduced electric field within the channel (50 Td) is far below the ionization threshold of air (120 Td). Reference [53] proposes a rough criterion for the streamer-to-spark transition in needle-to-needle electrodes: if the electric field within the channel exceeds the breakdown field, the streamer-to-spark transition may occur throughout the channel. Reference [29] provides a more conservative estimate for needle-to-plane electrodes, suggesting that a streamer-to-spark transition occurs only when the Laplacian field near the cathode exceeds the ionization threshold of air. Regardless of which criterion is applied, at this stage the applied voltage is still insufficient to transition to spark, and thus the streamer channel begins to expand laterally. Using a voltage of 129 kV as an example, 50 ns after the streamer bridges the gap, the electron-impact ionization reaction rate at the gap center (r = 0, z = 20 mm) is found to have decreased significantly:

$$e^- + N_2 \rightarrow N_2^+ + 2\,e^-\text{：}\ 1.51\times10^{24}\ \mathrm{m^{-3}\ s^{-1}}$$

$$e^- + O_2 \rightarrow O_2^+ + 2\,e^-\text{：}\ 6.18\times10^{24}\ \mathrm{m^{-3}\ s^{-1}}$$

In contrast, attachment, recombination, and quenching reactions dominate:

$$e^- + O_2 + O_2 \rightarrow O_2^- + O_2\text{：}\ 2.07\times10^{25}\ \mathrm{m^{-3}\ s^{-1}}$$

$$O_2^- + O_4^+ + N_2 \rightarrow O_2 + O_2 + O_2 + N_2\text{：}\ 3.66\times10^{25}\ \mathrm{m^{-3}\ s^{-1}}$$

$$O(^1D) + O_2 \rightarrow O + O_2\text{：}\ 6.51\times10^{26}\ \mathrm{m^{-3}\ s^{-1}}$$

$$O(^1D) + N_2 \rightarrow O + N_2\text{：}\ 1.52\times10^{27}\ \mathrm{m^{-3}\ s^{-1}}$$

The rate of new electron generation decreases and cannot compensate for electron losses. Meanwhile, electrons are captured to form O_2^-, which neutralizes with O_4^+ to produce neutral molecules, and excited $O(^1D)$ is quenched, rapidly dissipating its excitation energy. The discharge transitions from an ionization-dominated stage to a decay stage dominated by attachment, recombination, and quenching.

The streamer discharge corresponds to a weak ionization stage, and the temperature rise is primarily due to the release of energy from electronically excited atoms and molecules into the gas via collisional relaxation, known as the fast gas heating mechanism (FGH) [54]. At this stage, the low voltage and reaction rates lead to a modest increase in gas temperature, with the heating region mainly confined near the electrode. Under 58 kV, 97 kV, and 129 kV, the streamer channel temperature rises from 300 K to 304.6 K, 305.4 K, and 306.2 K, respectively. These results are consistent with the gas temperature measured from the $N_2(C^3\Pi_u)$ molecular spectra in Section 3.1.2.

The simulation results in this section show that the duration of electron depletion varies under different lightning impulse voltages, indicating that the slow rise time of the lightning impulse has a certain influence on streamer initiation. At 129 kV, a high reaction rate region emerges near the anode, which may be associated with the formation of secondary streamers. In addition, the simulations reveal that streamer evolve from a stage dominated by molecular excitation and energy transfer, to one dominated by ionization, and finally to a decay stage dominated by recombination and quenching. The calculated temperature rise within the streamer channel is only a few kelvin, which is in good agreement with the OES measurements.

3.2.2 Transition mechanism from streamer to spark discharge under lightning impulse

When the ionization front passes the point (r = 0, z = 20 mm), the E/N input is switched from the self-consistent result of the 2D model to a prescribed Laplacian field. The resulting discontinuity in E/N(t) induces a sudden jump in electron density. Although this jump is not strictly physically accurate, it nonetheless provides the necessary initial-condition information for the analysis of subsequent stages.

Fig 14 shows the temporal evolution of electron density and gas temperature under the voltage of 58 kV. Owing to the low reduced electric field, the electron density initially rises slowly and then gradually decays to the order of 10^{16} m^{-3}, ultimately failing to initiate spark.

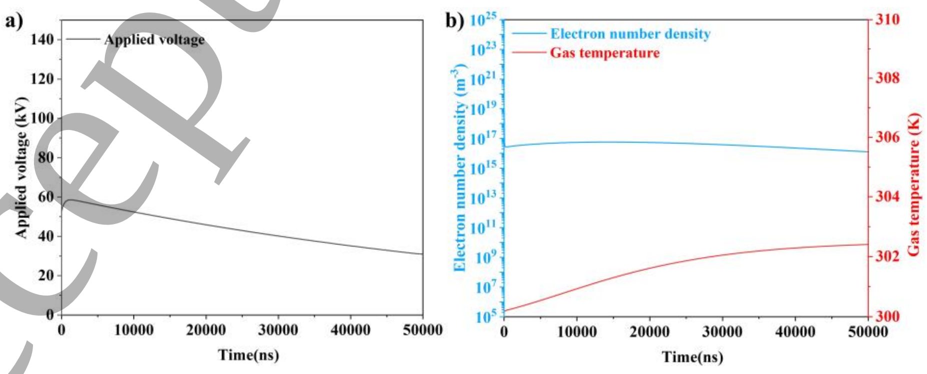

Fig 14. Variation of applied voltage, electron number density, and gas temperature at 58 kV. The time 0 on each axis corresponds both to the start of the 0D model and to the moment when the ionization front passes the probe point (r = 0, z = 20 mm) in the 2D model.

Figure 15 shows the reaction pathways of electron production and loss at 58 kV, inferred from the simulation results. O and O_3^- both serve as key reactants in the electron-producing reactions. The primary source of O is the dissociation reactions induced by energy transfer from the excited-state species $N_2(A^3\Sigma_u^+)$, $N_2(B^3\Pi g)$, $N_2(a'^1\Sigma_u^-)$ and $O_2(B^1\Sigma g^+)$. The production of O_3^- is 95% due to the three-body association of O^- with O_2 in the presence of a neutral third body, and to the reaction of O_2^- with O_3. Because the concentration of O is much higher than that of O_3^-, after the streamer, high-density O detaches electrons from negatively charged species (such as O_3^- and O_2^-) via reactions R1 and R2. These detachment reactions play a crucial role in sustaining the electron density under conditions of weak electric field or low gas temperature. At the same time, the attachment reaction between O_2 and low-energy electrons (R10) represents the primary pathway for electron loss. The resulting O_2^- continuously “cycles” through the O_4^- ion channel, thereby partially maintaining the overall stability of the negative ion concentration.

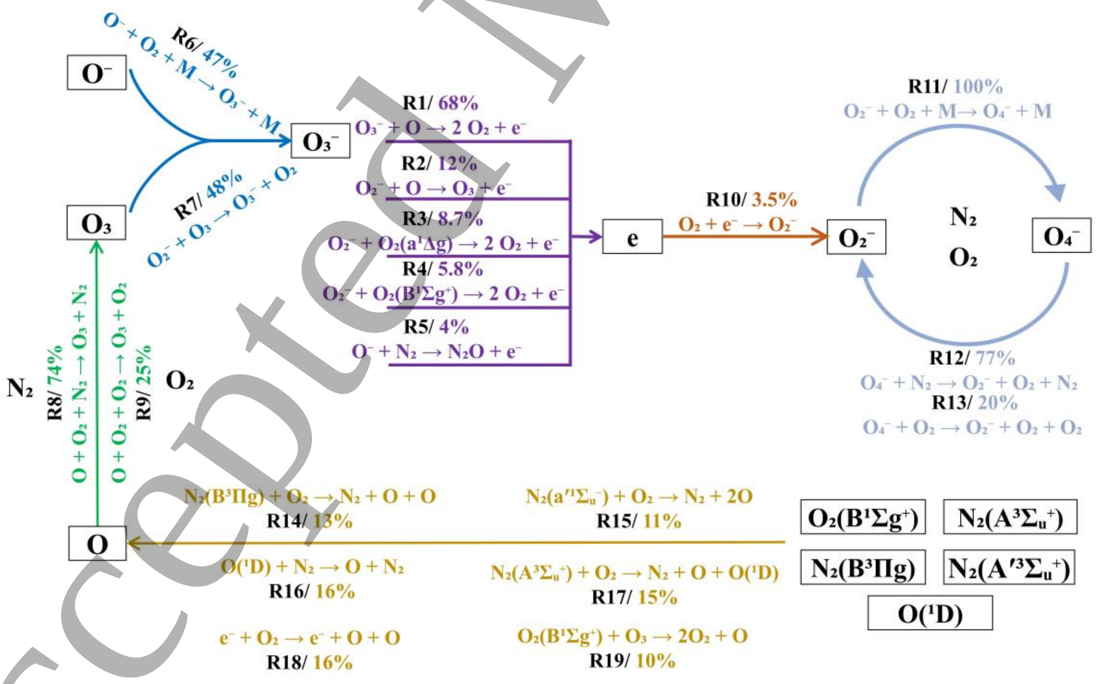

Fig 15. Main reaction pathways influencing electron density over the 0-50 000 ns under the voltage of 58 kV. Arrows indicate the direction toward products; reactions are labeled “R”; percentages denote each reaction’s contribution to product formation.

As shown in Fig 16 and 17, When the applied peak voltage increases from 58 kV to 97 kV, a transition from streamer to spark occurs in the 0D model. Furthermore, as the voltage increases from 97 kV to 129 kV, the transition time becomes significantly shorter. In the following, the case of 97 kV is taken as an example to analyze the streamer-spark transition mechanism, which is divided into three stages according to the growth rate of electron density.

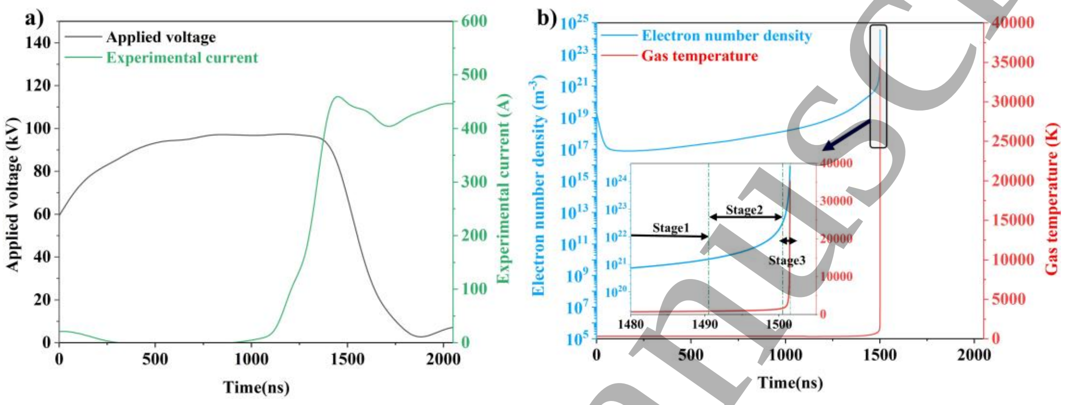

Fig 16. Variation of applied voltage, experimental current, electron number density, and gas temperature at 97 kV. (a) The time 0 on each axis corresponds both to the start of the 0D model and to the moment when the ionization front passes the probe point (r = 0, z = 20 mm) in the 2D model. The applied voltage and experimental current are obtained from experimental measurements. (b) The electron density and gas temperature are derived from numerical simulations.

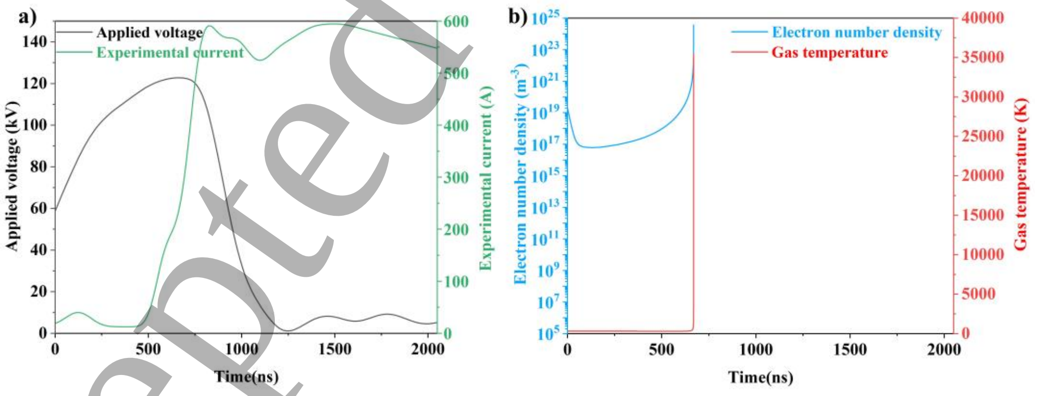

Fig 17. Variation of applied voltage, experimental current, electron number density, and gas temperature at 129 kV. (a) The time 0 on each axis corresponds both to the start of the 0D model and to the moment when the ionization front passes the probe point (r = 0, z = 20 mm) in the 2D model. The applied voltage and experimental current are obtained from experimental measurements. (b) The electron density and gas temperature are derived from numerical simulations.

Fig 18 shows the pathway analysis results over the 0-1490.5 ns under the voltage of 97 kV. During this stage, the electron density increases from 1.96×10^{19} to $1.55\times$

10^{21} m^{-3}, and the gas temperature further rises from 300.12 K to 870.24 K. When the voltage is increased, electrons gain higher energy. In addition to O detaching electrons from O^-, O_2^-, and O_3^-, direct ionization reactions R24 and R21 also become major sources of electrons. At the same time, reactions R10, R26, and R25 collectively dominate the electron loss process. Approximately 99 % of O^- is produced by R26 and R25, serving as the primary source of negative ions during electron detachment.

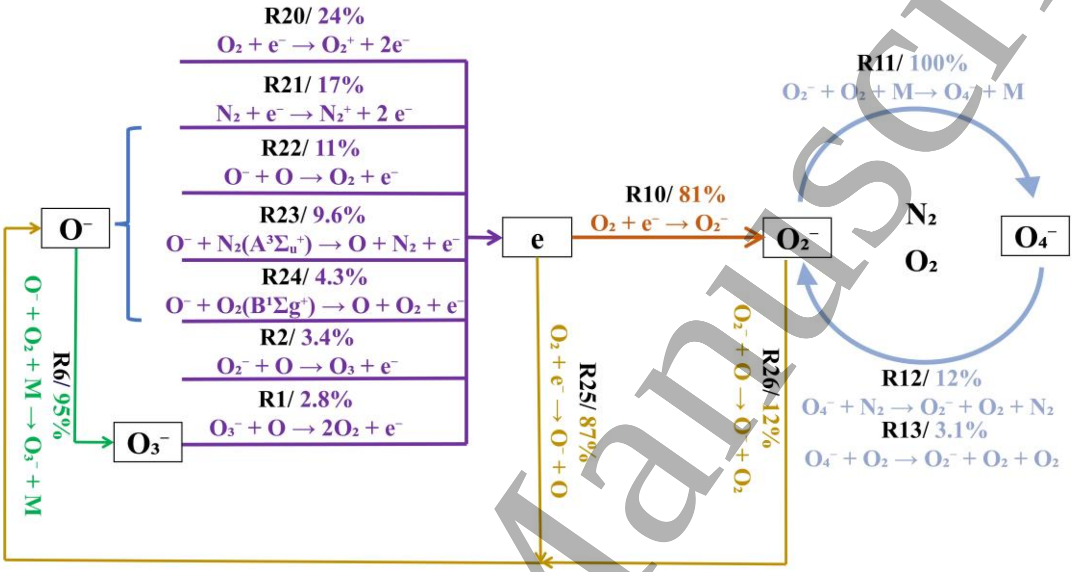

Fig 18. Main reaction pathways influencing electron density over the 0-1490.5 ns under the voltage of 97 kV. Arrows indicate the direction toward products; reactions are labeled "R"; percentages denote each reaction's contribution to product formation.

Subsequently, the interval from 1490.5 to 1500.5 ns is analyzed, during which the electron density increases from 1.55×10^{21} to 3.27×10^{22}m^{-3}, and the gas temperature further rises from 870.24 K to 1665.98 K. As shown in Fig 19, direct ionization processes R21 and R20 remain the primary electron-producing pathways. However, the ionization rates of molecular excited states $N_2(a'^1\Sigma_u^-)$, $N_2(C^3\Pi_u)$, and $O_2(a^1\Delta g)$, as well as atomic excited states $N(^2D)$, $O(^1S)$, $O(^1D)$, and $N(^4D^o)$, gradually increase, indicating a trend toward supplanting ground-state molecular ionization as the dominant electron-generation mechanism. Because the ionization cross-sections of excited-state species exceed those of ground-state species, their ionization rate constants are several orders of magnitude higher [39, 40]. Accordingly, as the concentrations of these excited-state species increase, the proportion of stepwise ionization in the overall ionization progressively rises. For diatomic molecules, excited states are prone to both dissociation and ionization. The resulting atoms can be rapidly excited and further ionized by electron impact. The resultant increase in electron density further promotes the ionization and dissociation of both ground-state and excited-state molecules, creating a positive feedback effect [20]. At this stage, owing to the elevated electron energies, dissociative recombination reactions (R35 and R36) together with the dissociative attachment reaction (R25) lead to electron loss and generate large quantities of neutral and excited-state atoms.

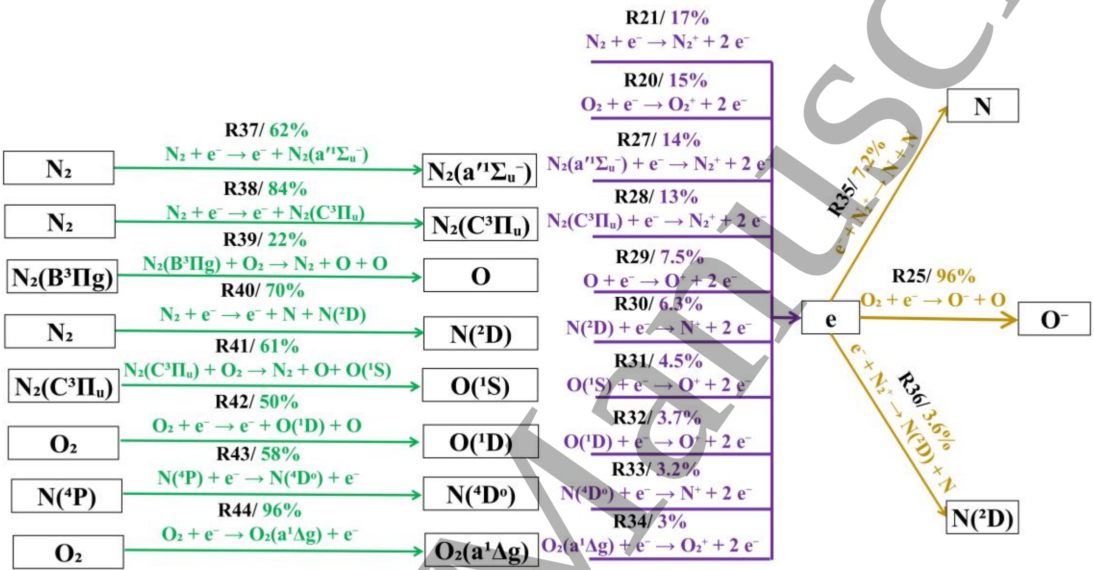

Fig 19. Main reaction pathways influencing electron density over the 1490.5-1500.5 ns under the voltage of 97 kV. Arrows indicate the direction toward products; reactions are labeled "R"; percentages denote each reaction's contribution to product formation.

Finally, the reaction pathways during the 1 ns preceding spark formation are analyzed (Fig 20). In this stage, the plasma composition undergoes a rapid transition from molecular to almost entirely atomic. The electron density swiftly rises from 3.27 $\times 10^{22}$ m^{-3} to 3.64 $\times 10^{24}$ m^{-3}, and the gas temperature increases from 1 665.98 K to 35 350 K. The simulation results are comparable to the experimentally measured electron density (9.51 $\times 10^{23}$ m^{-3}) and gas temperature (38 875 K) reported in Section 3.1.2. As shown in Fig 20, ionization of atomic excited states($N(^2D)$, $N(^4D^o)$, and $O(^1D)$) and ground-state oxygen atoms accounts for 45.8 % of the electron sources, far exceeding the 25.7% contribution from molecular ionization of $N_2(a'^1\Sigma_u^-)$, $N_2(C^3\Pi_u)$, and $N_2(B^3\Pi g)$. Consequently, N^+ and O^+ become the predominant charged species, which explains the experimental observation of spark emission spectra being dominated by atomic ion lines such as N^+ and O^+. As the degree of ionization increases, elastic electron-ion collisions become the dominant gas heating mechanism, with the thermalization time closely related to the electron density [20]. Due to the extremely high electron density in the final stage, the gas temperature rises by several tens of thousands of kelvins within just 1 ns. This study primarily focuses on the transition from streamer to spark discharge, while the stages following spark formation are beyond the scope of this work.

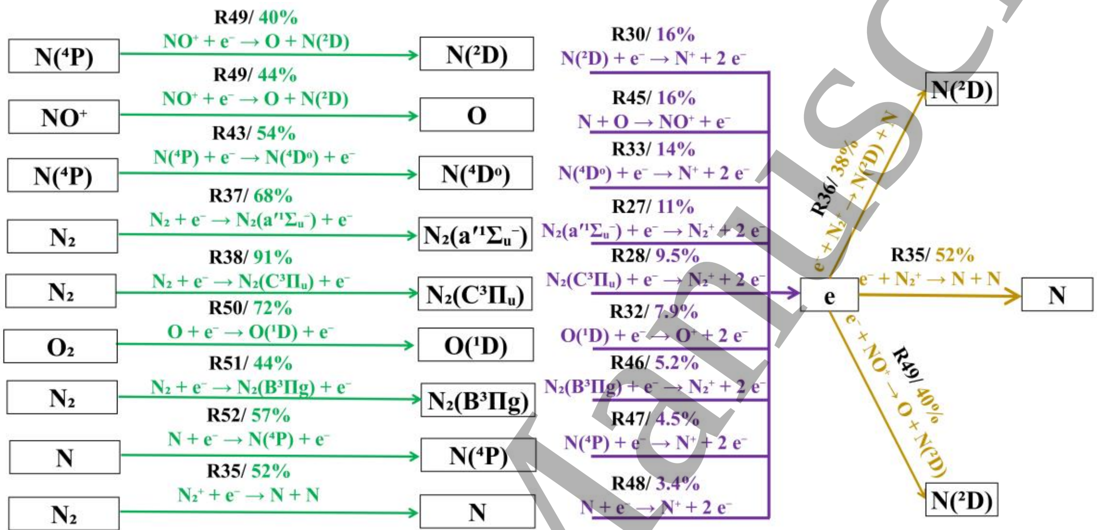

Fig 20. Main reaction pathways influencing electron density over the 1500.5-1501.5 ns under the voltage of 97 kV. Arrows indicate the direction toward products; reactions are labeled “R”; percentages denote each reaction’s contribution to product formation.

5. Conclusion

This study, based on an ultrafast electro-optical combined diagnostic platform and a 2D-0D coupled model, systematically investigates the discharge process of synthetic air in a 40-mm rod-plane gap at 0.1 MPa under lightning impulse.

Experimentally, compared with previous studies, several results and more detailed information are obtained. The results show that, under lightning impulse, the streamer channels in the 40-mm rod-plane gap may not all appear at the same moment due to the stochastic nature of the discharge. With increasing voltage, the streamer channels become significantly thicker and brighter, and the transition time from streamer to spark shortens from the microsecond to the sub-microsecond scale. At 58 kV, only streamer is observed, characterized by pronounced N_2(C-B) emission and low gas temperatures of 302.84-342.76 K, reflecting a typical non-equilibrium feature. At higher voltages of

97 kV and 129 kV, the discharge develops into the spark stage, accompanied by strong N^+ and O^+ emission lines, with the gas temperature rising to about 3.9×10^4 K and the electron density approaching the order of 10^{24} m^{-3}.

From the simulation perspective, the contribution of this work lies in introducing a 2D-0D discharge model coupled with the external circuit, which realistically reproduces the main evolution process of short-gap discharges under lightning impulse. The long rise time of the lightning impulse induces significant electron depletion within the gap, thereby affecting the streamer initiation process. Streamer initially occurs in a stage dominated by molecular excitation and energy transfer, then gradually transitions to ionization-dominated propagation, and finally enters a decay stage governed by attachment, recombination, and quenching. During the streamer-to-spark transition, at low voltage (58kV), electrons are mainly generated through negative ion detachment, while electron loss is dominated by attachment reactions. At higher voltages (97 kV and 129 kV), contributions from excited molecules and atoms to the ionization process are significantly enhanced. The electron density rises rapidly to 3.6×10^{24} m^{-3} within 1 ns, and the gas temperature increases to 3.5×10^4 K, marking the formation of the spark stage. More importantly, the simulations provide the distributions of electron density and gas temperature at different discharge stages, which are in good agreement with the experimental observations.

In summary, this study obtains results and conclusions from both experiments and simulations, which not only deepen the understanding of the discharge mechanisms of synthetic air under lightning impulse but also provide useful references for the insulation design of short gaps in GIS. Future work will further investigate the effects of different gas pressures, electrode gap lengths, and trace amounts of moisture, with the aim of more comprehensively elucidating the discharge processes under lightning impulse and promoting the application and optimization of synthetic air in high-voltage equipment.

References

[1] Inami K, Yoshida T, Hama H, et al. Partial discharge and breakdown properties in dry air, N, and CO under nonuniform electric field[J]. IEEE Transactions on Dielectrics and Electrical Insulation, 2023, 30(6): 2583-2591.

[2] Wu P, Li Y, Xiao S, et al. SnO2 nanoparticles based highly sensitive gas sensor for detection of C4F7N: A new eco-friendly gas insulating medium [J]. Journal of hazardous materials, 2022, 422: 126882.

[3] Seeger M, Stoller P, Garyfallos A. Breakdown fields in synthetic air, CO_2, a CO_2/O_2 mixture, and CF 4 in the pressure range 0.5 – 10 MPa[J]. IEEE Transactions on Dielectrics and Electrical Insulation, 2017, 24(3): 1582-1591.

[4] Rabie M, Franck C M. Assessment of eco-friendly gases for electrical insulation to replace the most potent industrial greenhouse gas SF_6[J]. Environmental science & technology, 2018, 52(2): 369-380.

[5] Tian S, Liu W, Ding J, et al. Study on subacute inhalation toxicity and offspring teratogenicity of C_4F_7N: An environmentally friendly insulating gas to replace SF_6[J]. Journal of Cleaner Production, 2023, 387: 135799.

[6] California Air Resources Board (CARB). Regulation for Reducing Sulfur Hexafluoride (SF_6) Emissions from Gas Insulated Equipment (GIE)[EB/OL]. California Code of Regulations, Title 17, Sections 95350–95359, 2021.

[7] European Parliament; Council of the European Union. Regulation (EU) 2024/573 of the European Parliament and of the Council of 7 February 2024 on fluorinated greenhouse gases, amending Directive (EU) 2019/1937 and repealing Regulation (EU) No 517/2014 [S]. Official Journal of the European Union, L 2024/573, 2024-02-20.

[8] Seeger M, Stoller P, Garyfallos A. Breakdown fields in synthetic air, CO_2, a CO_2/O_2 mixture, and CF_4 in the pressure range 0.5-10 MPa[J]. IEEE Transactions on Dielectrics and Electrical Insulation, 2017, 24(3): 1582-1591.

[9] Lim D-Y, Bae S. Study on oxygen/nitrogen gas mixtures for the surface insulation performance in gas insulated switchgear [J]. IEEE Transactions on Dielectrics and Electrical Insulation, 2015, 22(3): 1567-1576.

[10] Change I P O C. Climate change 2007: the physical science basis [J]. Agenda, 2007, 6(07): 333.

[11] Siddiqui N, Weeks C, Rogers J. Advancements in clean air insulation technologies for switchgear and circuit breakers [J]. IEEE Power and Energy Magazine, 2022, 20(2): 132-138.

[12] Park H, Lim D-Y, Bae S. Partial discharge and surface flashover characteristics with O2 content in N2/O2 mixed gas under a non-uniform field [J]. IEEE Transactions on Dielectrics and Electrical Insulation, 2018, 25(4): 1403-1412.

[13] Kosse S, Nikolic P G, Kachelriess G. Holistic evaluation of the performance of today's SF_6 alternatives proposals [J]. CIRED 24, 2017, 2017(1): 210-213.

[14] Lim D-Y, Bae S. Study on oxygen/nitrogen gas mixtures for the surface insulation performance in gas insulated switchgear [J]. IEEE Transactions on Dielectrics and Electrical Insulation, 2015, 22(3): 1567-1576.

[15] Loeb L B, Meek J M. The mechanism of the electric spark[M]. Stanford University Press, 1941.

[16] Shirvani A, Schufft W, Pampel H P, et al. Spatial-temporal investigation of breakdown of long air gaps by lightning voltages up to 2.4 MV[C]//2013 IEEE Electrical Insulation Conference (EIC). IEEE, 2013: 351-355.

[17] Zeng R, Chen S. The dynamic velocity of long positive streamers observed using a multi-frame ICCD camera in a 57 cm air gap[J]. Journal of Physics D: Applied Physics, 2013, 46(48): 485201.

[18] Subhana A, Støa-Aanensen N S, Gammelsæter M, et al. Lightning impulse testing in short air-gaps and memory effect of previous discharges[J]. IEEE Transactions on Dielectrics and Electrical Insulation, 2024, 31(5): 2485-2493.

[19] Chen X, Zhu Y, Wu Y. Modeling of streamer-to-spark transitions in the first pulse and the post discharge stage[J]. Plasma Sources Science and Technology, 2020, 29(9): 095006.

[20] Zhang B, Zhu Y, Zhang X, et al. Streamer-to-filament transition in pulsed nanosecond atmospheric pressure discharge: 2D numerical modeling[J]. Plasma Sources Science and Technology, 2023, 32(11): 115014.

[21] Minesi N, Mariotto P, Pannier E, et al. The role of excited electronic states in ambient air ionization by a nanosecond discharge[J]. Plasma Sources Science and Technology, 2021, 30(3): 035008.

[22] Meng Y, Xuan H, Deng Z, et al. The surface flashover process under positive lightning impulse voltage: initial stage and evolution[J]. Journal of Physics D: Applied Physics, 2022, 55(38): 385203.

[23] Ma X, Bai L, Zhu Y, et al. Numerical investigation of discharge evolution and breakdown characteristics of ArF excimer lasers[J]. Plasma Sources Science and Technology, 2024, 33(7): 075012.

[24] Yifei ZHU, Xiaochi MA, Luying BAI, Yifan QIU, Yun WU: PASSKEy2 code [software]. Available from http://www.plasma-tech.net/passkey2/passkey2/, Xi’ an Jiaotong University and Gongfang Tech Co, Ltd., China, 2024).

[25] Yifei ZHU, Xiancong CHEN, Yun WU, Pierre Tardiveau. Simulation of the ionization wave discharges: a direct comparison between the fluid model and E--FISH measurements. Plasma Sources Sci. Technol. (2021).

[26] Zhu Y, Shcherbanev S, Baron B, et al. Nanosecond surface dielectric barrier discharge in atmospheric pressure air: I. measurements and 2D modeling of morphology, propagation and hydrodynamic perturbations[J]. Plasma sources science and technology, 2017, 26(12): 125004.

[27] Zhu Y, Starikovskaia S. Fast gas heating of nanosecond pulsed surface dielectric barrier discharge: spatial distribution and fractional contribution from kinetics[J]. Plasma Sources Science and Technology, 2018, 27(12): 124007.

[28] Hagelaar G J M, Pitchford L C. Solving the Boltzmann equation to obtain electron transport coefficients and rate coefficients for fluid models[J]. Plasma sources science and technology, 2005, 14(4): 722.

[29] Chen X, Zhu Y, Wu Y. Modeling of streamer-to-spark transitions in the first pulse and the post discharge stage[J]. Plasma Sources Science and Technology, 2020, 29(9): 095006.

[30] Zhu Y, Wu Y, Wei B, et al. Nanosecond-pulsed dielectric barrier discharge-based plasma-assisted anti-icing: modeling and mechanism analysis[J]. Journal of Physics D: Applied Physics, 2020, 53(14): 145205.

[31] Li Z, Yang Z, Xu Y, et al. Study on the influence of temperature on positive streamer under sub-atmospheric pressure[J]. Journal of Physics D: Applied Physics, 2025, 58(19): 195201.

[32] Meyer H K H, Marskar R, Gjemdal H, et al. Streamer propagation along a profiled dielectric surface[J]. Plasma Sources Science and Technology, 2020, 29(11): 115015.

[33] Tochikubo F, Komuro A. Review of numerical simulation of atmospheric-pressure non-equilibrium plasmas: streamer discharges and glow discharges[J]. Japanese Journal of Applied Physics, 2021, 60(4): 040501.

[34] Wenjun N, Hao S, Xueming S, et al. Numerical investigation on the discharge formation in micrometer pores in structured catalyst irradiated by a helium atmospheric pressure plasma jet[J]. Plasma Sources Science and Technology, 2024, 33(2): 025004.

[35] Guo Y, Li Y, Zhu Y, et al. A numerical and experimental study on positive diffusive ionization waves in different N_2/O_2 mixtures: the role of photoionization[J]. Plasma Sources Science and Technology, 2023, 32(2): 025003.

[36] Pancheshnyi S, Eismann B, Hagelaar G, et al. ZDPlasKin: a new tool for plasmachemical simulations[J]. Bulletin of the American Physical Society, 2008, 53.

[37] Qiu Y, Zhu Y, Wu Y, et al. Numerical investigation of the hybrid pulse-DC plasma assisted ignition and NOx emission of $NH_3/N_2/O_2$ mixture[J]. Combustion and Flame, 2023, 258: 113078.

[38] Mao X, Rousso A, Chen Q, et al. Numerical modeling of ignition enhancement of CH4/O2/He mixtures using a hybrid repetitive nanosecond and DC discharge[J]. Proceedings of the Combustion Institute, 2019, 37(4): 5545-5552.

[39] Bacri J, Medani A. Electron diatomic molecule weighted total cross section calculation: III. main inelastic processes for N_2 and N_2^+[J]. Physica B+C, 1982, 112(1): 101-118.

[40] Wang Y, Zatsarinny O, Bartschat K. B-spline R-matrix-with-pseudostates calculations for electron-impact excitation and ionization of nitrogen[J]. Physical Review A, 2014, 89(6): 062714.

[41] Guo Y, Nijdam S. Statistical analysis on branching characteristics of positive streamer discharges in N_2-O_2 mixtures[J]. Plasma Sources Science and Technology, 2024, 33(4): 045006.

[42] Nijdam S, Van De Wetering F, Blanc R, et al. Probing photo-ionization: experiments on positive streamers in pure gases and mixtures[J]. Journal of Physics D: Applied Physics, 2010, 43(14): 145204.

[43] Seeger M, Avaheden J, Pancheshnyi S, et al. Streamer parameters and breakdown in CO_2[J]. Journal of Physics D: Applied Physics, 2016, 50(1): 015207.

[44] Li X, Guo B, Sun A, et al. A computational study of steady and stagnating positive streamers in N_2-O_2 mixtures[J]. Plasma Sources Science and Technology, 2022, 31(6): 065011.

[45] P. Felsenthal and J. M. Proud, “Nanosecond-pulse breakdown in gases,” Phys. Rev., vol. 139, A1796-A1804, 6A Aug. 1965.

[46] Julian Held. Julian-Held/OES-toolbox: v0.3.3. Zenodo; 2024.

[47] Lo A, Cessou A, Lacour C, et al. Streamer-to-spark transition initiated by a nanosecond overvoltage pulsed discharge in air[J]. Plasma Sources Science and Technology, 2017, 26(4): 045012.

[48] Minesi N, Stepanyan S, Mariotto P, et al. Fully ionized nanosecond discharges in air: the thermal spark[J]. Plasma Sources Science and Technology, 2020, 29(8): 085003.

[49] Konjević N, Lesage A, Fuhr J R, et al. Experimental Stark widths and shifts for spectral lines of neutral and ionized atoms (a critical review of selected data for the period 1989 through 2000) [J]. Journal of Physical and Chemical Reference Data, 2002, 31(3): 819-927.

[50] Shea J J. Physics of pulsed breakdown in gases[J]. IEEE Electrical Insulation Magazine, 2002, 17(5): 60-61.

[51] Pai D Z, Lacoste D A, Laux C O. Nanosecond repetitively pulsed discharges in air at atmospheric pressure—the spark regime[J]. Plasma Sources Science and Technology, 2010, 19(6): 065015.

[52] Zheng X, Sun Z, Li C, et al. Temporal evolution and mechanism of secondary streamers in N2/O2 mixtures at atmospheric pressure under DC voltage[J]. Journal of Physics D: Applied Physics, 2023, 57(12): 125203.

[53] Tholin F, Bourdon A. Influence of temperature on the glow regime of a discharge in air at atmospheric pressure between two point electrodes[J]. Journal of Physics D: Applied Physics, 2011, 44(38): 385203.

[54] Popov N A, Starikovskaia S M. Relaxation of electronic excitation in nitrogen/oxygen and fuel/air mixtures: fast gas heating in plasma-assisted ignition and flame stabilization[J]. Progress in Energy and Combustion Science, 2022, 91: 100928.

Data availability statement

The data that support the findings of this study are available upon reasonable request from the authors.

Acknowledgments

This work was supported by the National Natural Science Foundation of China (Nos. U23A20652 and 52507187).